Toroidal modelling of plasma response and RMP field penetration

Y.Q. Liu[1], A. Kirk[1], Y.Sun[2], P. Cahyna[3], I.T. Chapman[1], P. Denner[1], G. Fishpool[1], A.M. Garofalo[4], J.R. Harrison[1], E. Nardon[5], and the MAST team

[1]*Euratom/CCFE Fusion Association, Culham Science Centre, Abingdon, OX14 3DB, UK*
[2]*Institute of Plasma Physics, Chinese Academy of Sciences, PO Box 1126, Hefei 230031, China*
[3]*Institute of Plasma Physics AS CR v.v.i., Association EURATOM/IPP.CR, Prague, Czech Republic*
[4] *General Atomics, San Diego, California, 92186-5608, USA*
[5]*Euratom/CEA Fusion Association, 13108 St Paul-lez-Durance, France*

Abstract. The penetration dynamics of the resonant magnetic perturbation (RMP) field is simulated in the full toroidal geometry, under realistic plasma conditions in MAST experiments. The physics associated with several aspects of the RMP penetration - the plasma response and rotational screening, the resonant and non-resonant torques and the toroidal momentum balance - are highlighted. In particular, the plasma response is found to significantly amplify the non-resonant component of the RMP field for some of the MAST plasmas. A fast rotating plasma, in response to static external magnetic fields, experiences a more distributed electromagnetic torque due to the resonance with continuum waves in the plasma. At fast plasma flow (such as for the MAST plasma), the electromagnetic torque is normally dominant over the neoclassical toroidal viscous (NTV) torque. However, at sufficiently slow plasma flow, the NTV torque can play a significant role in the toroidal momentum balance, thanks to the precession drift resonance enhanced, so called superbanana plateau regime.

PACS numbers: 52.35.Py, 28.52.Av, 52.55.Fa, 52.65.Kj

1. Introduction

It is expected that large scale, low frequency type-I edge localized modes (ELMs) may not be tolerable for the plasma facing components in ITER, due to the large heat load [1]. Extensive experimental results from recent years, on several existing tokamak devices, have demonstrated that the externally applied resonant magnetic perturbation (RMP) fields can significantly affect the behavior of ELMs [2, 3, 4, 5]. It appears that the ELM mitigation/suppression, and the accompanying density pump-out effect observed in experiments, require detailed investigations due to complex physics. One important aspect is to understand the RMP field penetration dynamics during ELM mitigation.

The RMP penetration is an essentially non-linear process. In the fluid approximation, this involves two key effects coupled to each other. One is the plasma response to the applied RMP field, where the plasma flow normally plays a role of screening the external field. The other is the flow damping by torques created by the applied (often static) RMP field acting on the plasma. Extensive theory and modeling work has been carried out to study each of these effects separately: the plasma response at a given rotation [6, 7, 8, 9, 10, 11] and the electromagnetic as well as the neoclassical toroidal viscous (NTV) torque produced by the plasma response to 3D external field [12, 13, 15, 14]. The non-linear coupling between the plasma response and the $\mathbf{j} \times \mathbf{b}$ torque induced momentum damping has been analytically investigated in a cylinder [16], and numerically modeled in a cylindrical geometry assuming various fluid models [17, 18]. Reference [19] considered the rotation braking also by the NTV torque, but again for a cylindrical plasma, and with several other simplified assumptions.

In this work, we apply the recently developed MARS-Q code [20] to simulate the RMP penetration dynamics for a MAST plasma. The MARS-Q code employs a full MHD, single fluid model for the plasma response, but in a full toroidal geometry. The MHD equations are solved, in time domain, together with the momentum balance equation for the toroidal flow of the plasma. Both the fluid $\mathbf{j}\times\mathbf{b}$ torque and the NTV torque, as the solution of the bounce averaged drift kinetic equation in a generic torus, are incorporated into the momentum equation as the sink terms.

We shall present the work in the following order. We first show physics results concerning each individual aspect of the four important ingredients for the RMP penetration: the linear plasma response, the $\mathbf{j}\times\mathbf{b}$ torque, the NTV torque, and the toroidal momentum balance. Finally we shall present the non-linear simulation results for MAST.

2. Plasma response to RMP fields

In this Section, we consider a linear plasma response to an externally applied RMP field. We seek a steady state response as the stationary solution of the perturbed single fluid full MHD equations in the presence of a source term, i.e. the RMP coil current. Either an ideal or a resistive plasma response is computed in the presence of a toroidal plasma flow. The full description of the formulation is found in Ref. [10]. Figure 1(a) shows one example of the RMP coil geometry, for a MAST single-null discharge 25075, in which the plasma is shifted downwards, being closer to the lower set of coils. For the modeling, the plasma edge near the separatrix is slightly truncated to yield a finite edge safety factor $q_a = 5.32$. This creates 12 rational surfaces (with 12 resonant poloidal harmonics $m = 4, 5, \ldots, 15$) for an $n = 3$ perturbation as shown in Fig. 1(b). Here n is the toroidal mode number.

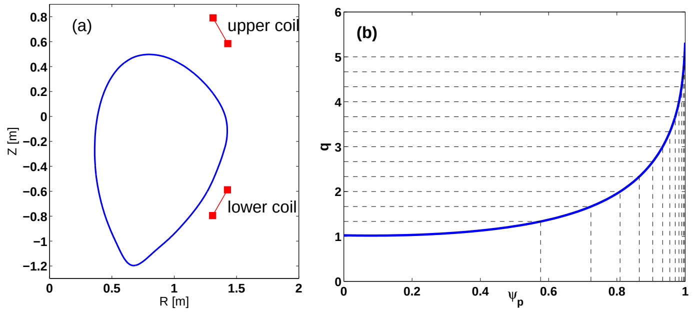

Figure 1: (a) The plasma boundary shape for the MAST lower SND discharge 25075 and the RMP coils; (b) the radial profile of the safety q, with dashed lines indicating the location of rational surfaces for the $n = 3$ field. ψ_p is the normalized equilibrium poloidal flux.

It has been previously found [11] that a resistive plasma response, in the presence of a fast toroidal flow, can provide a strong screening to the resonant harmonics of the RMP field. For this MAST plasma, the initial flow speed (before applying the RMP field) is about 4.8% of the Alfvén speed at the plasma centre. The amplitude of the resonant harmonics is reduced by 1-2 orders of magnitude, at the radial location of the corresponding rational surfaces, compared to that of the vacuum field components. This is indicated by the deep valley in the plasma response field spectrum shown in Fig. 2(b), where the radial field is defined as $b^1 \equiv q\mathbf{b}\cdot\nabla\psi_p/(R_0^2\mathbf{B}_{\rm eq}\cdot\nabla\phi)$ and Fourier decomposed in a straight-field-line flux coordinate system. Here R_0 is the major radius of the magnetic axis, $\mathbf{B}_{\rm eq}$ the equilibrium magnetic field, and ϕ the geometric toroidal angle.

On the other hand, computations show that this MAST plasma amplifies significantly the non-resonant harmonics that have the same sign of the field pitch as the resonant harmonics, i.e. the $m > 0$ harmonics shown in the figure. The amplitude of the resonant harmonics outside the rational surface is also amplified. The peak amplification factor is about 3 compared to the

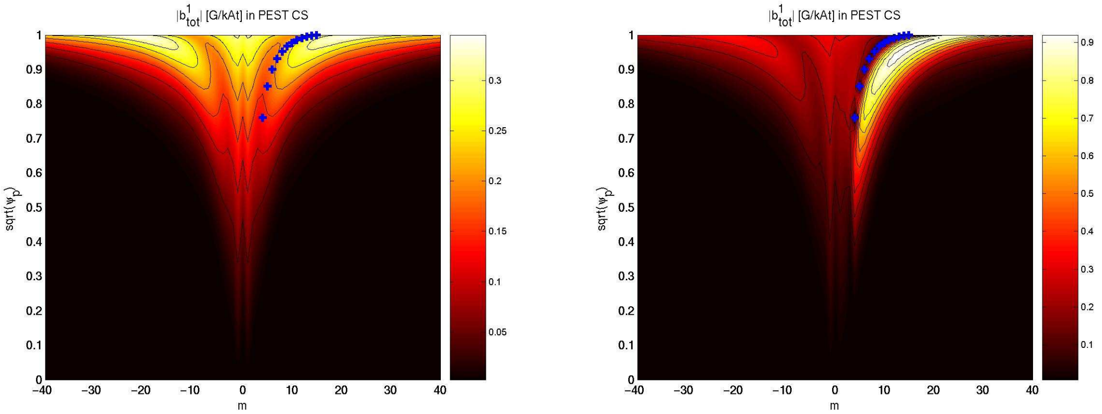

Figure 2: Comparison of the computed spectra of (a) the free space radial magnetic field produced by the RMP coil currents, and (b) the field including the plasma response. m numbers the poloidal Fourier harmonic decomposed in a straight-file-line flux coordinate system, with the flux surface labeled by ψ_p. The color coding shows the amplitude of the radial field b^1 (as defined in the text) in Gauss/kAt. The symbol "+" indicates the location of the $q = m/n$ rational surfaces, with $n = 3$.

vacuum field. Similar effect has been reported for DIII-D plasmas [21]. For the non-resonant harmonics with the opposite pitch ($m < 0$), the amplification is minor. This is typical for plasmas in RMP experiments.

Another important aspect of the plasma response is the formation of helical plasma surface displacement. These low$-n$ 3D displacements, with sufficient amplitude, may modify the local stability of high-n MHD modes [22, 23]. The MARS-Q computed plasma surface displacement is about 10mm for the MAST plasma-coil configuration ($n = 3$ at 5.6kAt coil current) shown in this example, quantitatively comparable to the experimental measurements [24]. We notice though that the steady state plasma displacement is sometimes sensitive to the equilibrium and in particular to the plasma flow speed.

The computed poloidal distribution of the amplitude of the plasma surface displacement also serves as a good indicator of the density pump-out effect observed in the MAST RMP experiments [11]. A detailed investigation showed that, at least in the fluid approximation, the density pump-out is associated with the excitation of the peeling-tearing like plasma response by the RMP fields, whilst in cases where no pump-out effect was observed, the plasma response exhibits more core-localized kink mode characteristics [11]. Extensive MARS-Q modeling also suggests that the poloidal distribution of the plasma surface displacement is sensitive to the plasma edge rotation.

3. Electromagnetic torque due to plasma response to static RMP fields

The electromagnetic torque is usually an important sink term in the toroidal momentum balance equation. The physics of the fluid electromagnetic resonant torque is well studied in the literature [16]. In addition to conventional understanding, recent toroidal modeling reveals two interesting regimes. One occurs at very slow plasma rotation frequency $\Omega \equiv \omega/\omega_A < \min\{S^{-1/3}|D_R|^{2/3}, S|D_R/\Delta_0'|^4\}$ as reported in Ref. [25], where ω denotes the angular frequency of the toroidal flow of the plasma, $\omega_A = V_{A0}/R_0$ the Alfvén frequency at the plasma center, with V_{A0} being the Alfvén speed V_A at the plasma center. S is the magnetic Lundquist number, D_R the resistive interchange index, and Δ_0' the tearing index calculated from the outer (ideal) region [26]. In this slow rotation case, the presence of a finite local pressure gradient at the rational surface introduces a strong screening effect of the external field, with *more* screening of amplitude of the resonant harmonics at *decreasing* toroidal rotation speed. This is due to the favorable average curvature effect - the same effect studied by Glasser, Greene and John [26] that leads to the enhanced tearing mode stability in a torus. This GGJ-term also results in a qualitative modification of the $\mathbf{j}\times\mathbf{b}$ torque at slow plasma flow, namely by producing a net accelerating force to the plasma flow (instead of a dragging force) [25].

In the other limit, of a fast plasma flow, the toroidal modeling results show a resonant splitting effect [27]. One example is shown below. For a clear illustration, we assume a large aspect ratio ($R/a = 10$) circular plasma with a parabolic radial profile for the equilibrium toroidal current density. The safety factor at the plasma center is $q_0 = 1.05$, and $q_a = 2.62$ at the plasma surface. There is only one rational surface $q = 2$ inside the plasma for the n=1 plasma response that is investigated here. The plasma has a finite pressure, such that both Alfvén and sound continuum waves are present in the plasma. In this case, the plasma response to an external static magnetic field (produced by the dc RMP coil currents) rotates in the plasma frame. The resonance conditions between the plasma rotation ω and the shear Alfvén wave $\omega^2 = \omega_a^2 \equiv \omega_A^2(m/q-n)^2/(\hat{\rho}F_{PS})$, the sound wave $\omega^2 = \omega_h^2 \equiv \omega_a^2 V_s^2/(V_s^2+V_A^2/F_{PS})$, respectively, create resonant surfaces that are located near the rational surface but are usually splitted into two surfaces (for each continuum resonance). Here $\hat{\rho} \equiv \rho/\rho_0$ is the plasma density ρ normalized by the central value ρ_0. V_s is the sound speed. Note that the Pfirsch-Shlutter inertial enhancement factor $F_{PS} = 1+q^2/(m-1-nq)^2+q^2/(m+1-nq)^2$ is explicitly included here to re-normalize the Alfvén speed.

One example is shown in Fig. 3(a), where several resonant surfaces are analytically predicted by the above resonant conditions, for a given (uniform) rotation frequency $\omega = 10^{-3}\omega_A$. The MARS-Q computed $\mathbf{j}\times\mathbf{b}$ torque density is plotted in Fig. 3(b), for the Lundquist number $S = 10^9$ and $S = 10^6$, respectively. A finite torque density is obtained at radial locations matching well the analytically predicted resonant surfaces. The torque density is well localized near these resonant surfaces at $S = 10^9$, though numerically well resolved by utilizing a strongly packed radial mesh. (An *a-posteriori* criterion based adaptive radial mesh refinement procedure is introduced into MARS-Q, in order to dynamically pack the mesh.) This resonant splitting effect also results in several surface-like plasma current sheets near a single rational surface, as shown by Fig. 3(c). At sufficiently small Lundquist number, these multiple current sheets tend to spread and form a more global radial distribution. The structure of the localized current sheets at $S = 10^9$, generated by the Alfvén continuum resonances and shown in Fig. 3(d), is qualitatively similar to that obtained in a cylindrical computation [17]. More detailed results of the continuum resonance induced $\mathbf{j}\times\mathbf{b}$ torque will be reported elsewhere [27].

With a larger plasma resistivity (which is often the case in the plasma edge region), the distribution of the torque density can become more global as shown in Fig. 3(b) for $S = 10^6$, even though only a single rational surface is present in this plasma. For a more realistic plasma equilibrium, where many rational surfaces exist inside the plasma, and are closely located to each other (typically near the plasma edge), one can expect a rather global distribution of the $\mathbf{j}\times\mathbf{b}$ torque density. One example will be shown in Fig. 6 for the MAST plasma.

4. NTV torque due to plasma response to 3D magnetic fields

The NTV torque is computed in MARS-Q, based on the analytic formulas that smoothly connect different collisionality regimes [12]. These analytic formulas are obtained by solving the bounce-averaged drift kinetic equation in a generic toroidal geometry, in various collisionality limits. Both non-resonant contribution and resonant contributions are included. The non-resonant NTV torque occurs at fast $\mathbf{E}\times\mathbf{B}$ flow. The resonant NTV contribution occurs when

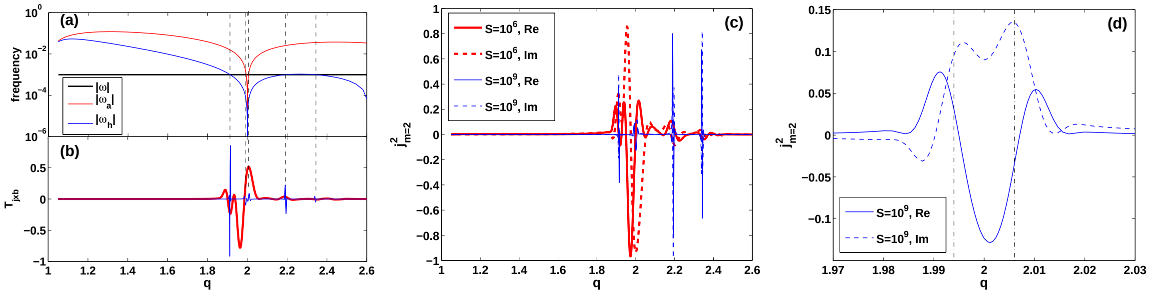

Figure 3: (a) The shear Alfvén (ω_a) and sound (ω_h) continua induced resonant surfaces (indicated by vertical dashed lines) appearing near a single, $q = 2$, rational surface in the presence of a finite, uniform toroidal rotation (ω). The computed electromagnetic torque density (b), and the poloidal component of the perturbed current inside the plasma (c), with the Lundquist number $S = 10^9$ (thin line) and $S = 10^6$ (thick line). (d) the radial distribution of the perturbed poloidal current density near the Alfvén resonance region, at $S = 10^9$. The vertical lines in (d) indicate the radial location of analytically estimated resonant surfaces.

the $\mathbf{E} \times \mathbf{B}$ flow speed is comparable to the precessional drift velocity of bulk plasma species. Three collisionality regimes are identified in each of non-resonant and resonant contributions. These are the so called $\nu-, \sqrt{\nu}-, 1/\nu-$ regimes for the non-resonant NTV torque, and the superbanana, superbanana plateau, $1/\nu-$ regimes for the resonant NTV torque. Normally the $\sqrt{\nu}-$ or the superbanana plateau regime gives the largest NTV torque, depending on the plasma flow speed.

In order to validate the NTV module in MARS-Q, we have performed systematic computations for a DIII-D plasma, where the non-axisymmetric magnetic field is generated by the I-coils (shown in Fig. 4(a)) in the n=3 configuration and dedicated experiments are carried out to measure the NTV torque [28]. An odd parity between the upper and lower sets of coils is chosen in experiments, producing almost purely non-resonant field components (consequently, the electromagnetic torque, produced by these coils on the plasma, is negligibly small, as also confirmed by MARS-Q computations).

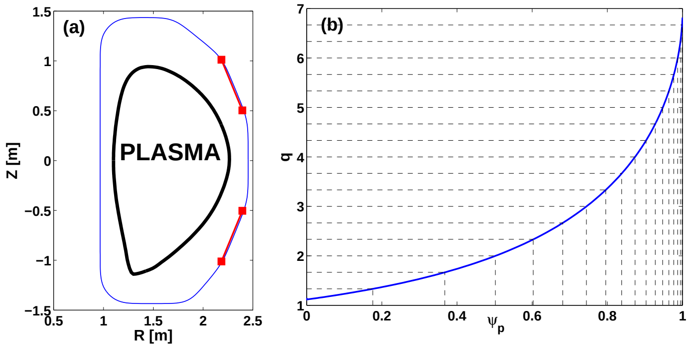

Figure 4: (a) The plasma boundary shape for a DIII-D plasma from discharge 138593. Shown are also the resistive wall shape and the I-coils mounted on the wall. (b) The radial profile of the safety factor q for this plasma is plotted, together with all rational surfaces ($n = 3$) indicated by dashed lines.

We compute the net NTV torques acting on the plasma for about 200 time slices, using the same coil configuration as in the experiment, and a plasma equilibrium reconstructed some-where in the middle of the time period. The experimental plasma equilibrium radial profiles (the plasma density, toroidal rotation, the thermal ion and electron temperatures) are used as the input to the NTV module at each time slice. An additional input is the $\mathbf{E}\times\mathbf{B}$ rotation frequency ω_E. Either the experimentally measured value $\omega_E^{\mathrm{EXPT.}}$ (dashed line in Fig. 5(a)) or that derived from neoclassical theory $\omega_E^{\mathrm{NEO.}}$ (dash-dotted line in Fig. 5(a)) are used. The MARS-Q computed NTV torque quantitatively agrees with experiments at later time of the discharge, as shown in Fig. 5(a). (The NTV torque is indirectly measured in experiments, involving the TRANSP runs.) The agreement is less satisfactory at the early time of discharge, when the plasma flow is fast, and the computed NTV torque is small compared to the experiment. Similar results are obtained by the IPEC code for this discharge [28].

The plasma rotation speed significantly drops at the later time of the discharge. At the slow rotation regime, the MARS-Q computed NTV torque agrees reasonably well with experiments. The computations show that the plasma enters into the superbanana plateau regime at this stage, as shown by the detailed analysis for the time at 3410ms (Fig. 5(b)). Note that the plasma collisionality above curve (3) corresponds to the $1/\nu$-regime; below (6) we have the ν-regime; below (5) we have the superbanana regime; between (6) and (3) is the $\sqrt{\nu}$-regime for the non-resonant NTV torque; and between (5) and (3) is the superbanana plateau regime for the resonant NTV torque. Curve (1) corresponds to the upper limit for the validity of the NTV theory used in these computations. The fact that curve (3) is largely below curve (2) indicates the significant resonance between the $\mathbf{E}\times\mathbf{B}$ flow and the thermal particle precession drifts which enhances the NTV torque. The resulting total torque mainly comes from the resonant contribution as shown by Fig. 5(c). The fact that the curve (4) is largely located between curve (3) and (5) indicates that this DIII-D plasma, at 3410ms, is in the superbanana plateau regime for the NTV torque.

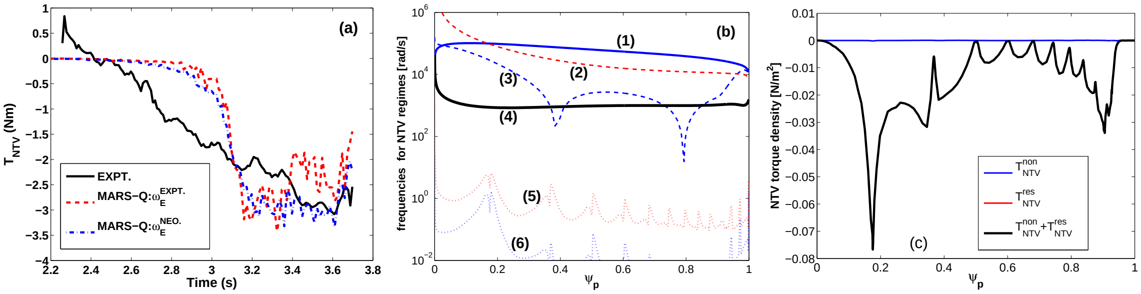

Figure 5: (a) Comparison between the computed NTV torque (dashed and dash-dotted lines) and the experiment (solid line), for the DIII-D discharge 138593. These are the plasma volume integrated net torques. (b) Various frequencies and boundaries between different collisionality regimes for the NTV torque for this DIII-D discharge at 3410ms: curve (1) represents $\sqrt{\varepsilon}\omega_{ti}$, where ε is the inverse minor radius, ω_{ti} is the thermal ion transit frequency; curve (2) represents ω_{D0}/ε, where ω_{D0} is the magnetic precession drift frequency of deeply trapped particles at thermal velocity; curve (3) represents the $\mathbf{E}\times\mathbf{B}$ frequency $|\omega_E|$; curve (4) represents the collision frequency ν/ε; curve (5) represents $\omega_{D0}(\delta B/\varepsilon)^{3/2}$, with δB being the amplitude of the surface-averaged perturbed magnetic field; curve (6) represents $|\omega_E|(\delta B/\varepsilon)^2$. (c) The computed non-resonant, resonant and total NTV torque at 3410ms. The curve for the resonant contribution nearly overlaps with that of the total torque.

The above results show the sensitive dependence of the NTV torque magnitude on the plasma rotation speed. This may be essential in interpreting the experimentally observed toroidal momentum damping, in particular in cases where both the electromagnetic $\mathbf{j}\times\mathbf{b}$ and the NTV torques contribute to the momentum sink. One example is shown in Fig. 6 for a MAST plasma. In this case, the RMP coils produce both resonant and non-resonant field components. At fast flow (Fig. 6(a)), which corresponds to the initial plasma flow of $\Omega = 4.8\%\omega_A$ at the plasma centre before applying the RMP field, the electromagnetic torque density amplitude is 1-2 orders of magnitude larger than the NTV torque density. [We also notice a rather global distribution of the $\mathbf{j}\times\mathbf{b}$ torque density, as a combined result of the presence of multiple rational surfaces for this MAST plasma, and the resonant splitting effect reported in Section 3. This globalization of the $\mathbf{j}\times\mathbf{b}$ torque density, with further enhancement from the radial diffusion of the toroidal momentum during the RMP field penetration, can potentially lead to a rather global damping of the toroidal flow.] The computed net total $\mathbf{j}\times\mathbf{b}$ torque is about -0.67Nm, compared to the net NTV torque of -0.03Nm. However, with a 10 times reduced plasma flow speed (Fig. 6(b)), the NTV and the $\mathbf{j}\times\mathbf{b}$ torques become comparable, with the net $\mathbf{j}\times\mathbf{b}$ torque of -2.42Nm and the net NTV torque of -1.36Nm. Note also that the dominant contribution (to the total NTV torque) comes from the non-resonant torque in the fast rotation case. Detailed analysis shown in Fig. 7(a) indicates that, in this case, the MAST plasma collisionality is mainly in the $\sqrt{\nu}$-regime. In the slow rotation case (Fig. 7(b)), the dominant contribution comes from the resonant NTV torque, and the plasma collisionality is in the boundary between the superbanana plateau and the $1/\nu$-regime.

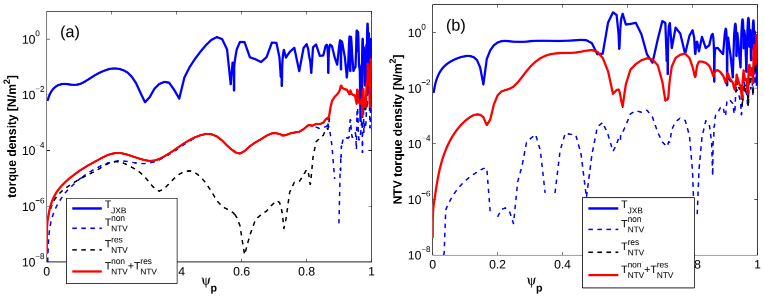

Figure 6: Comparison of the computed $\mathbf{j}\times\mathbf{b}$ and NTV torque densities for the MAST plasma from discharge 25075 at (a) initial flow speed before applying the RMP field, and (b) 10 times smaller flow speed. The linear, steady state plasma response to the lower set of 12 RMP coils at 5.6kAt in the $n = 3$ configuration is computed.

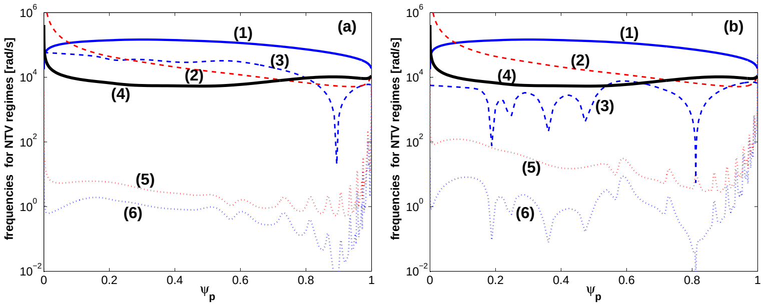

Figure 7: Various frequencies and boundaries between different collisionality regimes for the NTV torque, for the MAST plasma from discharge 25075 at (a) initial fast rotation before applying the RMP field, and (b) 10 times reduced rotation speed. The curves represent the same physical quantities as in Fig. 5. The linear, steady state plasma response to the lower set of 12 RMP coils at 5.6kAt in the $n = 3$ configuration is used to estimate the boundaries between the ν- and the $\sqrt{\nu}$-regimes, as well as between the superbanana and the superbanana plateau regimes.

5. Toroidal momentum balance

In the MARS-Q modeling of the RMP field penetration, the toroidal flow speed is determined self-consistently from solving the toroidal momentum balance equation

$$\frac{\partial L}{\partial t} = \frac{G}{s}\frac{\partial}{\partial s}\frac{s}{G}\left[\chi_M < |\nabla s|^2 > \frac{\partial L}{\partial s} + V_{\rm pinch} < |\nabla s| > L\right] + T_{j\times b} + T_{NTV}(\omega_E) + T_{\rm source}, \tag{1}$$

where $L = \rho < R^2 > \Omega$ is the toroidal moment, $G \equiv F < 1/R^2 >$ a geometrical factor. s labels the radial coordinate, F is the equilibrium poloidal current flux function, χ_M the (anomalous) toroidal momentum diffusion coefficient, and $V_{\rm pinch}$ the pinch velocity. The quantities χ_M and $V_{\rm pinch}$ are chosen in an *ad-hoc* manner in our model. For the non-linear simulations presented in this work, we choose the χ_M value corresponding to several m^2/s, which is the value for a typical MAST plasma. We neglected the pinch term in the modeling.

The momentum balance equation is subject to an initial condition, and two boundary conditions at the plasma center and surface. If we start the simulation at the time ($t = 0$) when the RMP coil current is switched on (neglecting the transit current ramp-up phase), and if the momentum source term $T_{\rm source}$ does not change during the application of the RMP field, we can solve for the change of the toroidal rotation, $\Delta\Omega = \Omega - \Omega(t = 0)$, instead of the total rotation Ω. In this case, the momentum source term, which is assumed to be balancing the momentum diffusion and pinch terms before applying the RMP field, drops out of the equation.

We assume the Neumann boundary condition $\partial(\Delta\Omega)/\partial s = 0$ at the plasma center, and the Dirichlet boundary condition $\Delta\Omega = 0$ at the plasma boundary surface. In principle, the boundary condition at the plasma edge should also involve the momentum exchange in the scrape-off layer. However, the Dirichlet condition is normally a reasonable approximation [16].

The toroidal momentum balance equation is solved using a finite element method along the minor radius. The details of the formulation, numerical implementation, as well as the benchmark results are reported in Ref. [20].

6. Non-linear modeling of RMP penetration

6.1. MARS-Q formulation

The MARS-Q formulation couples the perturbed MHD equations with the toroidal momentum balance equation (1) [20]. The MHD equations assume the single-fluid approximation with a generic toroidal plasma flow, and are solved together with the vacuum equation, the coil current equation (the source term for the RMP field), as well as the magnetic flux diffusion equation for the resistive wall (when applicable). In the following, these coupled equations are symbolically written as

$$\begin{aligned} B\frac{\partial X}{\partial t} &= A_1 X + Y A_2 X + X_0, \\ C\frac{\partial Y}{\partial t} &= DY + T(Y)X^2, \end{aligned}$$

where the first equation denotes the MHD equations. the second equation denotes the momentum balance ($Y \equiv \Delta\Omega$). The source term (RMP coil current) is denoted by X_0.

We have implemented a semi-implicit, adaptive time stepping scheme to solve the above coupled system of equations [20]. The first equation (MHD operators) is treated fully implicitly. The linear operator of the second equation (momentum diffusion and pinch terms) is also treated implicitly, whilst the quadratic terms (the $\mathbf{j} \times \mathbf{b}$ and the NTV torques) are evaluated using the values from the previous time step. These two coupled equations are solved on a staggered time-mesh.

6.2. Modeling results for a MAST plasma

The full toroidal simulation of the RMP field penetration, within the MARS-Q model, brings together all the ingredients discussed in previous Sections. We show the modeling results on an example of the MAST plasma described by Fig. 1. In this case, we consider only the lower set of 12 coils in the $n = 3,4,6$ configurations (the upper coils are far from the plasma, and hence have much smaller effect on the plasma). The coil current is 5.6kAt, the same as in experiments. A resistive plasma model is assumed, with the magnetic Lundquist number $S = 3.5 \times 10^7$ in the plasma center, and the radial profile determined by $S \propto T_e^{3/2}$ (the S value at the plasma edge is about 10^6). The fully implicit scheme for the MHD operators allows us to take large time steps. The adaptivity in time, shown in Fig. 8, follows the rate of the change of the full solution of the coupled equations. In the initial stage, when the solution changes rapidly, the scheme tends to reduce the time step. The time step is progressively increased (decreased) as the solution starts to evolve slowly (rapidly). An upper limit, of $500\tau_A$ for this simulation, is posed to the time step as a numerical parameter, where τ_A is the Alfvén time, which is 0.795μs for this MAST discharge.

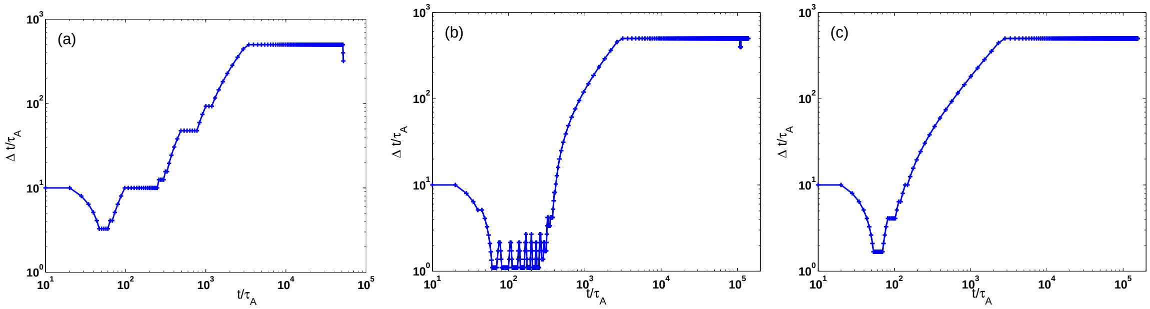

Figure 8: Adaptive time stepping obtained during the RMP field penetration simulation with the $n = 3,4$ and 6 coil configurations, respectively.

Figure 9 compares the simulated evolution of the radial profiles for the toroidal rotation. Only profiles at 21 selected time slices are shown in each case, with the interval between each time slice of about 2ms, 5.5ms and 6ms, for the $n = 3,4,6$ configurations, respectively. With the $n = 3$ configuration, at about 40ms after switching on the RMP coils, the toroidal rotation is nearly fully damped across a significant portion of the plasma column. On the other hand, the $n = 4$ and 6 coil configurations result only in a partial braking of the toroidal flow. Note that the Dirichlet boundary condition prevents the plasma edge rotation to vanish in these simulations (the initial rotation has a finite but small rotation frequency at the plasma edge). The time traces of the rotation frequency at rational surfaces are compared in Fig. 10 between the simulations and the MAST experiments. The simulation saturates at finite rotation frequencies for the $n = 4$ and 6 configurations, whilst a full braking of the rotation at rational surfaces is obtained with the $n = 3$ coils. Similar observations (and time scales) have been made in experiments. For the $n = 3$ case, further time stepping leads to unphysical results without additional non-linear physics (e.g. the magnetic island saturation). We notice a slight discrepancy between the assumed initial rotation frequency in MARS-Q modeling, and the experimental value at 0.27s. This is largely due to the fact that the RMP current ramp-up phase is not modeled in MARS-Q, whilst the experimental data shown here correspond to the flat RMP current phase.

The computed final rotation profiles after the RMP field penetration are compared in Fig. 11(a)

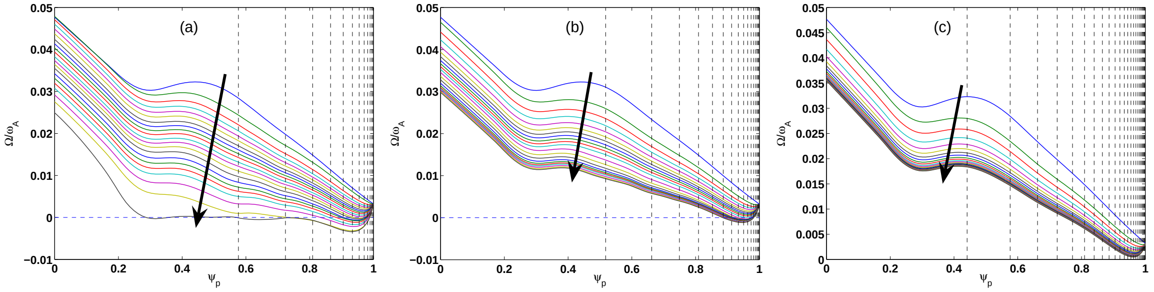

Figure 9: The simulated radial profile evolution of the toroidal rotation frequency during the RMP field penetration, for the $n = 3, 4$ and 6 coil configurations, respectively. Only selected profiles are plotted, at the time interval of about 2ms, 5.5ms and 6ms for $n = 3, 4$ and 6, re

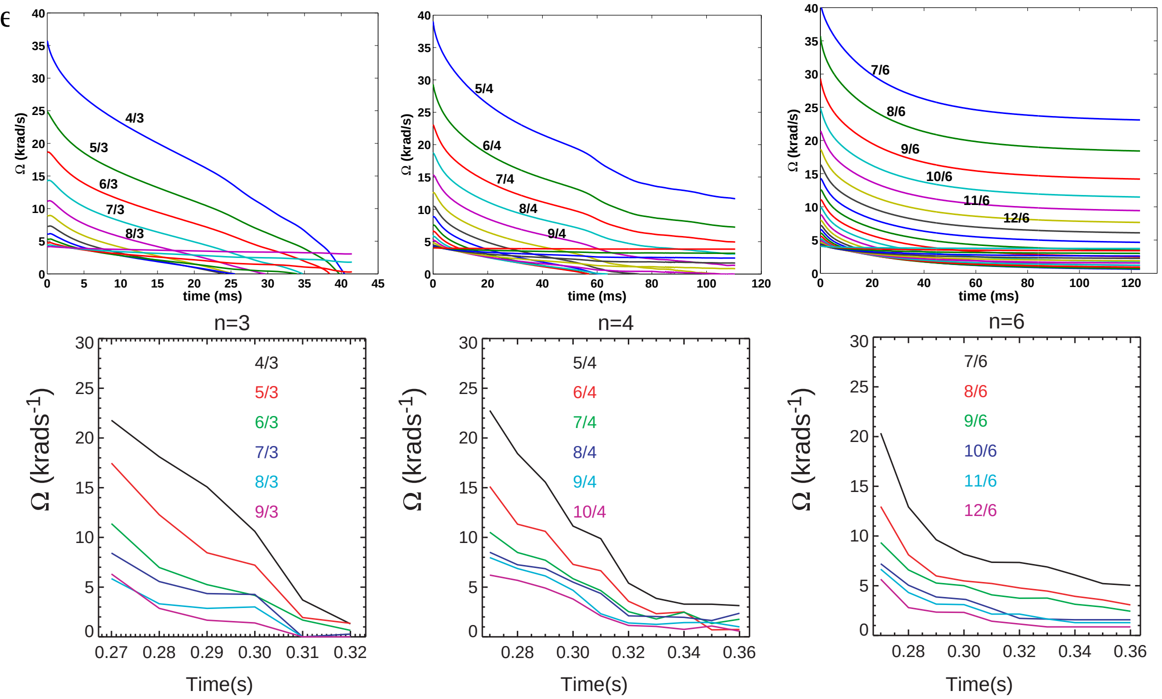

Figure 10: Comparison between the simulated time traces (upper panels) of the rotation braking and the MAST experiments (lower panels). Plotted are the toroidal rotation frequencies at rational surfaces during the RMP field penetration, for the $n = 3, 4$ and 6 coil configurations, respectively.

between the $n = 3, 4$ and 6 coil configurations. Due to the diagnostic limitation (the charge exchange recombination spectroscopy, which measures the toroidal rotation speed, is located at the mid-plane of the vacuum chamber, whilst the plasma is shifted downwards in these experiments), no core rotation data are available from experiments, for $\psi_p < 0.16$. The initial rotation profile at $\psi_p < 0.16$ is also obtained by a free boundary cubic spline extrapolation based on experimental data.

On the other hand, the simulation predicts that, with the $n = 3$ RMP field, a finite central plasma rotation still remains at the time of the full braking of the rotation elsewhere. The radial profile evolution of the plasma rotation depends on the choice of the profile for the momentum diffusion coefficient χ_M. Figure 11(b) compares the simulated rotation profiles after the RMP field penetration for the $n = 3$ configuration, with three different momentum diffusion profiles $\chi_M(s) = \chi_{M0}s^p$, with the power factor $p = 0, -1, -2$, respectively (the default choice is $p = -1$). The value of χ_{M0} is chosen to match the neoclassical prediction, which is about 3m^2/s for the MAST plasmas [29]. As expected, increasing of momentum diffusion in the plasma

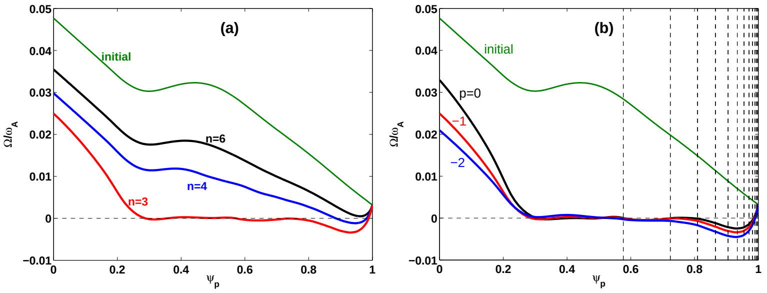

Figure 11: (a) Comparison of the final rotation profiles after the RMP field penetration, between the $n = 3,4,6$ cases. The simulations start with the same initial rotation for $n = 3,4,6$. (b) The simulated final rotation profiles after the $n = 3$ RMP penetration, with three choices of the momentum diffusivity profile.

core region helps to brake the core rotation.

It is interesting to compare the time traces of the net $\mathbf{j} \times \mathbf{b}$ and NTV torques, shown in Fig. 12, during the field penetration. For the $n = 3$ configuration, at the initial stage (with fast plasma flow), the electromagnetic torque plays the dominant role in the momentum sink. As the simulation approaches the full rotational braking, the NTV torque becomes the dominant factor whilst the $\mathbf{j} \times \mathbf{b}$ torque vanishes. The latter observation can be analytically demonstrated in a cylinder, with or without a finite equilibrium pressure [16, 25]. For the $n = 4$ configuration, the $\mathbf{j} \times \mathbf{b}$ and NTV torques become comparable at saturation. For the $n = 6$ configuration, however, the net NTV torque is still much smaller than the $\mathbf{j} \times \mathbf{b}$ torque even at the steady state. Generally, the combined total torque with the $n = 4$ and 6 configurations is smaller than that of the $n = 3$ configuration, which explains a weaker momentum damping with the former.

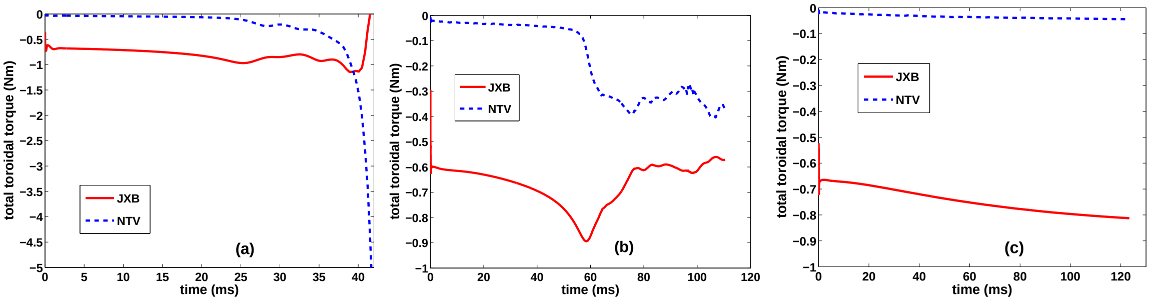

Figure 12: The simulated time traces of the net electromagnetic and NTV torques during the RMP field penetration, for the $n = 3,4$ and 6 coil configurations, respectively.

Figure 13 plots the amplitude of the radial component of the resonant harmonics at the corresponding rational surfaces for the $n = 3,4,6$ cases separately. The vacuum RMP field, the linear steady state response with the initial plasma flow (before applying the RMP field), and the final solution after the simulated RMP penetration are compared for each case. The penetrated field is still smaller than the vacuum field, but larger than that from the linear response with initial flow (the screened field). In particular, a significant penetration of the resonant field into the plasma core is achieved for the $n = 3$ case, which probably explains the full damping of the toroidal flow. The penetration of the $n = 4$ and 6 fields is still limited to the plasma edge region after the saturation, explaining the partial braking of the plasma rotation.

During the RMP field penetration, the plasma surface displacement is also recorded and shown in Fig. 14. Similar to the results of the linear response computations, the progressively increasing X-point peaking seems to correlate with the field penetration.

7. Summary and discussion

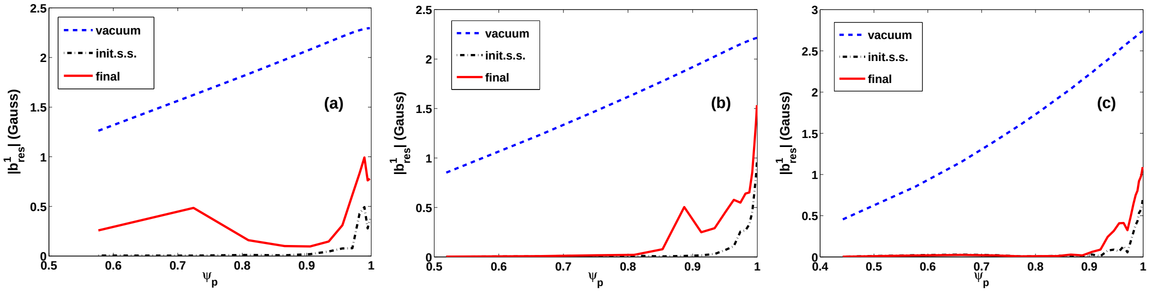

Figure 13: Comparison of the amplitude of the resonant harmonics of the radial magnetic field at corresponding rational surfaces, for the vacuum field (dashed), the linear steady state plasma response with the initial plasma flow (dash-dotted), and the final magnetic field from the non-linear penetration simulations. Shown are for the $n = 3,4$ and 6 coil configurations respectively.

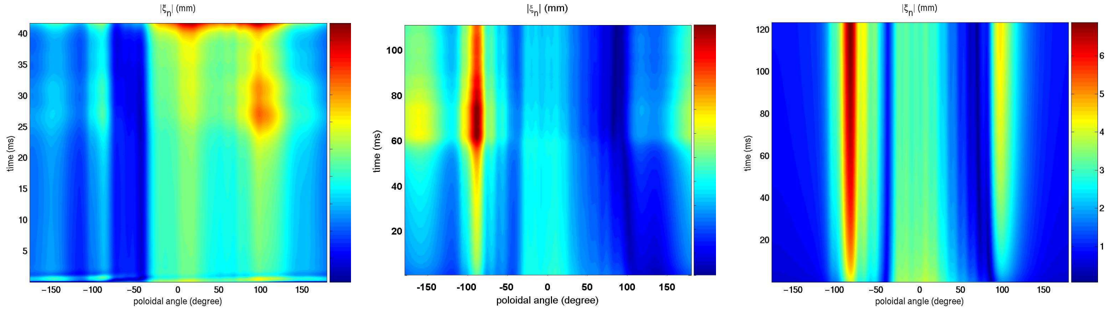

Figure 14: Evolution of the amplitude of the plasma surface displacement (the normal component) along the poloidal angle (defined in an equal-arc flux coordinate system), during the non-linear simulation of the $n = 3,4$ and 6 RMP field penetration, respectively.

The RMP field penetration process involves several important aspects: the plasma response to the RMP field in the presence of flow shielding from the plasma; the damping of the plasma flow due to momentum sinks such as the electromagnetic and the neoclassical toroidal viscous forces; the axisymmetric momentum balance; and finally the non-linear interplay between these components.

We have separately investigated the physics involved in each of the components, before presenting a full toroidal modeling of the RMP field penetration in a MAST plasma, under realistic experimental conditions.

When the plasma response is treated perturbatively (i.e. linear, steady state solution of a driven system), we found a strong screening of the resonant harmonics of external fields by a fast toroidal flow of the plasma. This screening is perfect by an ideal plasma - the amplitude of resonant harmonic vanishes at the corresponding rational surface. For a toroidal, resistive plasma under realistic conditions, the screening often provides 1-2 orders of magnitude reduction of the resonant harmonics with sufficiently fast plasma flow. At very slow plasma flow, on the other hand, the favorable average curvature term, which is responsible for the tearing mode stabilization in a torus, can provide a strong screening effect on the RMP field.

Contrary to the screening of resonant harmonics (at rational surfaces), the toroidal plasma response often amplifies the non-resonant harmonics, as well as the resonant harmonics outside rational surfaces. This is demonstrated in a MAST plasma from the RMP experiments, where an amplification factor of about 3 is obtained for the non-resonant harmonics with the same sign of magnetic pitch (i.e. $m > 0$ assuming $n > 0, q > 0$) as the resonant ones. The non-resonant harmonics with the opposite pitch ($m < 0, n > 0, q > 0$) experiences only a moderate amplification in these RMP plasmas.

Another interesting aspect associated with the linear, steady plasma response to helical external fields, is the generation of a 3D plasma displacement. The computed amplitude of the plasma surface displacement is of order of 10mm for MAST plasmas at 5.6kAt RMP coil current with the n=3 configuration. These values are quantitatively comparable to experimental measurements in MAST. An earlier study for MAST also found that the poloidal distribution of the plasma displacement has an intrigue correlation with the density pump-out effect observed in the RMP experiments.

The MARS-Q modeling also reveals interesting physics of the electromagnetic torque, depending on the plasma rotation regime. At a slow plasma rotation, the so called GGJ-term qualitatively alters the fluid $\mathbf{j} \times \mathbf{b}$ torque, by reversing the sign of the net torque. On the other hand, the response of a fast rotating plasma to a static external field produces the resonant splitting effect, as a result of the resonance between the rotating response, in the plasma frame, and the continuum waves in the plasma. Both shear Alfvén wave and sound wave contribute to the resonant splitting. As a result, the surface-like perturbed parallel current, which is responsible for the screening, occurs at several radial locations near the (single) rational surface. This splitting effect also effectively re-distributes the electromagnetic torque along the plasma minor radius, resulting in a more globally distributed $\mathbf{j} \times \mathbf{b}$ torque density, as opposed to the conventional understanding of the rational-surface-localized electromagnetic torque. This torque spreading becomes more pronounced with increasing the plasma resistivity.

The NTV module in MARS-Q, based on the analytic formulas that smoothly connect all collisionality regimes in the NTV theory, produces results that, at relatively slow plasma flow, are in quantitative agreement with experimental measurements in one of the DIII-D non-resonant magnetic field discharges. The dominant contribution of the NTV torque in this case comes from the so called superbanana plateau regime, in which the torque is significantly enhanced by the resonance between the $\mathbf{E} \times \mathbf{B}$ flow and the precessional drifts of bulk plasma species. At fast plasma rotation, however, the MARS-Q computed NTV torque is smaller than the experimental measurements in DIII-D. Further investigation is needed, from both the theory and the experimental sides, in order to resolve this discrepancy. Despite this discrepancy at fast plasma flow, a reasonably good quantitative agreement is obtained between the MARS-Q modeling and the MAST experiments, for the toroidal rotation braking. This is partly due to the fact that the NTV contribution is relatively small at fast plasma flow, as also shown by the DIII-D experiments.

The fast plasma rotation in MAST often excludes the possibility of the superbanana plateau regime. In stead, the collisionality condition of the MAST plasma considered here results in the so-called $\nu - \sqrt{\nu}$ regime. The net torque is still 1-2 orders of magnitude smaller than the net $\mathbf{j} \times \mathbf{b}$ torque. However, with the progressive braking of the plasma flow with the application of the RMP fields, it is possible to enter the superbanana plateau regime also for MAST plasmas. In this case, the resulting NTV torque can be comparable to the fluid $\mathbf{j} \times \mathbf{b}$ torque.

MARS-Q employs an adaptive, semi-implicit time stepping scheme to solve the coupled MHD-momentum balance equations. The latter includes both the momentum source and sink terms (i.e. the electromagnetic and the NTV torques), as well as the momentum diffusion and pinch terms. The toroidal momentum balance equation is solved using a finite element method along the plasma minor radius.

A simulation of the RMP field penetration, with the inclusion of all the above elements, is performed for a MAST RMP plasma. With 5.6kAt of the lower set of 12 coils in the n=3 configuration, the MARS-Q simulation predicts a full damping of the toroidal rotation, at about 40ms after application of the RMP fields. These results re-produce well the experimental observations. The modeling also reveals that the predominant damping force is produced by the electromagnetic torque in the initial phase of the RMP field penetration. However, after the RMP field is well penetrated, and the plasma flow is well damped, the electromagnetic torque diminishes, and the predominant role of the toroidal momentum damping is played by the NTV torque in this MAST discharge.

The above results imply that, for the ELM mitigation using the RMP field, such as that envisaged in ITER, it may be important to choose a proper toroidal spectrum of the applied field. On one hand, we need to choose low n number(s) to have sufficiently large field in the plasma region; on the other hand, too low n field (e.g. n=3 in MAST) may completely suppress the plasma flow. A finite flow is often essential for both stability and confinement of the tokamak plasma. The MAST experiments demonstrate that, with higher n (n=4 or 6) RMP fields, it is possible to mitigate ELMs while still maintaining a finite plasma rotation. Quantitative prediction of the RMP penetration and the flow damping for ITER plasmas will be carried out using MARS-Q.

We emphasize that the plasma response, that we considered in this work, refers to the *perturbed* response. In other words, the MARS-Q computed final 3D state in the presence of the RMP field does not correspond to the truly steady state, dynamically accessible 3D equilibrium. The validity of the perturbative results lies in the assumption that the applied 3D field is much smaller than the plasma equilibrium field. However, even in this case, the perturbative approach may be questionable near plasma rational surfaces (or the splitted resonant surfaces) where a large surface current is generated.

In this work, only toroidal flow is considered, which is responsible for the RMP field screening observed in the modeling. It has also been pointed out that the poloidal flow (more precisely the flow perpendicular to the equilibrium field lines) can play a crucial role for the RMP field screening [18]. This effect will be investigated in a full toroidal geometry, with an updated version of MARS-Q in the future. Since the electron flow seems to be important in the field screening [7], it may also be important to consider the two-fluid approximation for the RMP penetration problem. The results presented here largely follow the single-fluid approximation, except for the NTV torque, which is derived by solving the bounce-orbit averaged drift kinetic equation.

Finally, the magnetic field line stochastisation (say, after the full penetration of the RMP field) can enhance the particle radial transport and give rise to an additional radial current [30]. The resulting $\mathbf{j} \times \mathbf{b}$ torque presents additional momentum sink/source term, which is not included in this study.

Acknowledgments. This work was part-funded by the RCUK Energy Programme under grant EP/I501045 and the European Communities under the contract of Association between EURATOM and CCFE. The views and opinions expressed herein do not necessarily reflect those of the European Commission.

References

[1] Loarte A *el al* 2007 *Nucl. Fusion* **47** S203

[2] Evans T E *et al* 2007 *Nat. Phys.* **2** 419
[3] Liang Y *et al* 2007 *Phys. Rev. Lett.* **98** 265004
[4] Kirk A *et al* 2011 *Plasma Phys. Control. Fusion* **53** 065011
[5] Suttrop W *et al* 2011 *Phys. Rev. Lett.* **106** 225004
[6] Waelbroeck F L 2003 *Phys. Plasmas* **10** 4040
[7] Heyn M F *et al* 2008 *Nucl. Fusion* **48** 024005
[8] Yu Q *et al* 2009 *Phys. Plasmas* **16** 042301
[9] Park G *et al* 2010 *Phys. Plasmas* **17** 102503
[10] Liu Y Q *et al* 2010 *Phys. Plasmas* **17** 122502
[11] Liu Y Q *et al* 2011 *Nucl. Fusion* **51** 083002
[12] Shaing K C *et al* 2010 *Nucl. Fusion* **50** 025022
[13] Park J K *et al* 2009 *Phys. Rev. Lett.* **102** 065002
[14] Sun Y *et al* 2010 *Phys. Rev. Lett.* **105** 145002
[15] Sun Y *et al* 2010 *Plasma Phys. Control. Fusion* **52** 10500
[16] Fitzpatrick R 1998 *Phys. Plasmas* **5** 3325
[17] Kikuchi Y *et al* 2006 *Nucl. Fusion* **48** 169
[18] Nardon E *et al* 2010 *Nucl. Fusion* **50** 034002
[19] Bécoulet M *et al* 2009 *Nucl. Fusion* **49** 085011
[20] Liu Y Q *et al* “Toroidal modeling of penetration of the resonant magnetic perturbation field” 2012 *Phys. Plasmas* submitted
[21] Lanctot M *et al* 2011 *Phys. Plasmas* **18** 056121
[22] Chapman I T *et al* 2010 *Phys. Rev. Lett.* **105** 255002
[23] Canik J *et al* 2012 *Nucl Fusion* in press
[24] Chapman I T *et al* “Three dimensional corrugation of the plasma edge when magnetic perturbations are applied for ELM control in MAST” 2012 *Plasma Phys. Control. Fusion* submitted
[25] Liu Y Q *et al* 2012 *Phys. Plasmas* **19** 072509
[26] Glasser A H *et al* 1975 *Phys. Fluids* **18** 875
[27] Liu Y Q *et al* “Continuum resonance induced electromagnetic torque by a rotating plasma response to static RMP field” 2012 *to be submitted*
[28] Garofalo A M *et al* 2011 *Nucl. Fusion* **51** 083018
[29] Baranov Yu F *et al* 2009 *Plasma Phys. Control. Fusion* **51** 044004
[30] Rozhansky V *et al* 2010 *Nucl. Fusion* **50** 034005